Research Square

Preprints are preliminary reports that have not undergone peer review.
They should not be considered conclusive, used to inform clinical practice,
or referenced by the media as validated information.

Lateral inputs sustains subsurface particle export during low productivity in Equatorial Atlantic

Joelle Habib

Joellehabib22@hotmail.com

Laboratoire d'océanographie de villefranche sur mer https://orcid.org/0000-0001-9604-7927

Lars Stemmann

Laboratoire d'océanographie de villefranche sur mer

Ajit Subramaniam

Columbia University https://orcid.org/0000-0003-1316-5827

Alberto Baudena

Consiglio Nazionale Delle Ricerche-Istituto di Scienze Marine

Ana Fernández-Carrera

Institute of Oceanography and Global Change / Universidad de Las Palmas de Gran Canaria

Claudeilton S. de Santana

GEOMAR Helmholtz Centre for Ocean Research Kiel

Franz Philip Tuchen

Institute of Environmental Physics, University of Bremen

Peter Brandt

GEOMAR Helmholtz Centre for Ocean Research Kiel https://orcid.org/0000-0002-9235-955X

Wokil Bam

School of Ocean Science and Engineering, University of Southern Mississippi https://orcid.org/0000-0002-7320-3496

Rainer Kiko

GEOMAR Helmholtz Centre for Ocean Research https://orcid.org/0000-0002-7851-9107

Article

Keywords:

Posted Date: March 12th, 2026

DOI: https://doi.org/10.21203/rs.3.rs-8935744/v1

License: This work is licensed under a Creative Commons Attribution 4.0 International License.
Read Full License

Additional Declarations: There is **NO** Competing Interest.

Lateral inputs sustain subsurface particle export during low productivity in Equatorial Atlantic

Joelle Habib[1], Lars Stemmann[1,2], Ajit Subramaniam[3], Alberto Baudena[1,4], Ana Fernández-Carrera[5], Claudeilton S. de Santana[6], Franz Philip Tuchen[7,8], Peter Brandt[6,9], Wokil Bam[10], Rainer Kiko[1,6,9].

[1]Sorbonne Université, CNRS, Laboratoire d'Océanographie de Villefranche, LOV, 06230 Villefranche-sur-Mer, France
[2]Institut Universitaire de France (IUF), Paris, France
[3]Lamont-Doherty Earth Observatory, Columbia University, Palisades, NY, USA
[4]Consiglio Nazionale Delle Ricerche-Istituto di Scienze Marine (CNR-ISMAR), Lerici (SP), Italy
[5]Institute of Oceanography and Global Change / Universidad de Las Palmas de Gran Canaria
[6]GEOMAR Helmholtz Centre for Ocean Research Kiel, Kiel, Germany
[7]Institute of Environmental Physics, University of Bremen, Bremen, Germany
[8]Now at: University of Miami, Rosenstiel School of Marine, Atmospheric & Earth Science, Miami, FL, USA
[9]Faculty of Mathematics and Natural Sciences, Kiel University, Kiel, Germany
[10] School of Ocean Science and Engineering, University of Southern Mississippi, Stennis Space Center, MS, USA

Abstract

The equatorial Atlantic Ocean is characterized by seasonal upwelling and complex nutrient dynamics. These processes shape the temporal and spatial distribution of primary productivity causing a pronounced east-west chlorophyll-*a* gradient. But whether this surface biomass pattern is reflected in particle production and export remains uncertain. We analyze vertical high-resolution particle size distribution data from Underwater Vision Profilers and physical oceanographic observations collected during two trans-Atlantic cruises conducted in contrasting seasons. During the higher productivity fall season, upwelling and tropical instability waves enhanced local primary production and supported deep export of large particles. In contrast, during the lower productivity boreal spring, unexpectedly high concentrations of small particles (0.1-0.5 mm) were observed in the central basin, concentrated within the Equatorial Undercurrent (EUC), which is supplied by the energetic North Brazil Current retroflection. Backward trajectory analysis and biological and hydrographic evidence suggest that these particles originate from the South American continental margin and are laterally transported eastward along a short advective pathway into the EUC. Estimating Particulate Organic Carbon (POC) flux from the particle size distributions, we find that during the low-productivity period, between 15-35°W, over 70% of the POC flux in the upper 200 m might be attributed to small particles (0.05-0.1mm) carried within the EUC. These findings highlight the importance of lateral subsurface transport for equatorial carbon cycling, thereby influencing deep-sea and benthic ecosystem structure.

Phytoplankton fix approximately 50 Pg of carbon annually in the oceans, accounting for nearly half of the global net primary production[1]. Much of this biomass is remineralized in the upper ocean, only 10–25% escape immediate recycling[2]. This export flux sustains a vertical CO_2 gradient, enhancing oceanic CO_2 sequestration through the biological carbon pump (BCP[3,4]).

Sinking of particulate organic matter (marine snow) is central to the BCP. Marine snow consists of detritus formed from organic particles aggregated by physical and biological processes[5]. Large marine snow aggregates (>500μm) efficiently transport carbon to depth[6–8] and are widely represented in models[9–12]. Recent studies show small particles (50 - 400 μm) contribute to 50% of the upper 1000 m particulate organic carbon (POC) flux [13–18].

Equatorial oceans are a critical component of the global carbon cycle due to their unique dynamics including seasonal upwelling, mixing and strong horizontal currents such as the Equatorial Undercurrent (EUC) among the strongest currents eastward equatorial currents, driving spatial and temporal variability in surface chlorophyll[19,20]. However, deeper in the ocean, studies of carbon biomass and export in these regions remain limited, primarily due to constraints in observational coverage. The Equatorial Atlantic (EA), with ~20% higher phytoplankton biomass in the euphotic zone than the equatorial Pacific[19], is thought to be a region of enhanced biological production and particulate carbon export associated with the BCP[21]. This productivity[20,22,23] fuels deep particulate flux[16,21] modulated by enhanced nutrient supply[24], through seasonal upwelling and mixing[25], horizontal advection[26], and intraseasonal variations such as tropical instability waves (TIWs)[27].

Seasonal variability at the Equator is dominated by an annual cycle of the EUC transport and core depth, and a semi-annual cycle in EUC core velocity with maxima in April and September [28–30]. The relative positioning of the nitracline and the EUC core varies seasonally and spatially[31]. From boreal summer to early winter in the eastern basin, the nitracline shoals above the EUC core, whereas during boreal spring, the EUC core is shallow across the basin, shaping seasonal and spatial patterns of productivity in the EA[19,24,32]. This structure produces an east-west chl-*a* gradient, with higher productivity in the east[20,26] and bloom events that have been linked to rapid carbon fluxes reaching depths of up to 4000 m[16,21]. The broader effect of this zonal productivity gradient on POC export is still unknown. This study's primary hypothesis assumes a spatial gradient in particle abundance and carbon export that aligns with the chlorophyll-*a* (chl-a) gradient, a common proxy for phytoplankton biomass.

We conducted two full-depth trans-Atlantic cruises using the Underwater Vision Profiler 5 (UVP5) in boreal fall 2019[33] and spring 2022[34] to study the equatorial particle dynamics (Fig. S1). The 2019 cruise (M158) took place at the end of the seasonal cooling, a period of relatively high nutrient supply and biological productivity (as indicated by satellite-derived Chl a concentrations; Brandt et al.[31]) and before a major warming event that peaked in January 2020[35]. The 2022 cruise (M181) occurred during the warm season, characterized by reduced nutrient supply and low chl-a concentrations[32] at the surface, following the Atlantic Niño that peaked in July 2021[36]. Both cruises were conducted outside major recent climatic anomalies in the EA. Contrary to our hypothesis, shipboard particle size measurements revealed unanticipated high concentrations of small particles during the less productive period in boreal spring, especially in the western EA. In this study, we investigate three potential mechanisms for the enhanced particulate carbon supply in the epi- and mesopelagic layers during M158 and M181: 1) seasonal upwelling, 2) TIWs, and 3) horizontal advection of suspended or slowly sinking particles from the continental margin via the North Brazil Current (NBC) retroflection and the EUC.

Physical processes shape primary productivity and carbon cycling

Seasonal variability in the EA controls nutrient supply and phytoplankton biomass[20] and moderate carbon export[37,38]. We find that during fall 2019, surface waters were relatively cool along the equatorial transect, with a minimum Sea Surface Temperature (SST) of 25°C between 5°W and 10°W marking the remnants of the equatorial cold tongue [39] (Fig. 1a). The 20°C isotherm, a proxy for the nitracline[24] based on model simulations showing heat-nutrient coupling, ranged between 100-140 m, and deepened westward.

Three upwelling regions were identified: (1) an eastern region (5-10°W) with an SST decrease of 2°C, surfacing of the 25°C isotherm (Fig. 1e), and satellite-derived chl-a reaching 0.5 mg m^{-3} extending westward to 18°W (Fig. 1c); (2) a central region (25-30°W) with chl-a up to 0.2 mg m^{-3} (Fig. 1c,g); and (3) a western region

(35-40°W), associated with a TIW front visible in satellite SST. This front induced a double chl-a peak in the upper 40 m (Fig. S2) consistent with previous observations[40]. During this period, nitrate-rich thermocline waters were located above the EUC core and diffused into the mixed layer[31] while TIW-driven vertical mixing and frontal processes provided additional nutrient inputs[41–43]. These inputs supported an increase in primary production, with integrated production derived from shipboard measurements, with a mean value of 496 ± 181 mg C m^{-2} d^{-1} at the eastern site (Fig. S3) declining westward to mean values of 388 ± 105 mg C m^{-2} d^{-1} in the central region and 344 ± 76 mg C m^{-2} d^{-1} in the west. Pigment markers suggest a relative dominance of nanoflagellates and cyanobacteria (Prochlorococcus, Synechococcus and/or Trichodesmium) in the communities (Fig. S4a-c).

In contrast, spring 2022 was characterized by weak upwelling (at 0°), low surface chl-a[31] and warm surface waters (29°C) along the EA before the onset of the Equatorial Cold Tongue (Fig. 1b). A weak shoaling of the thermocline between 0° and 5°W induced minor surface cooling. Surface chl-a was low in the west, the eastern transect (0–5°W) showed higher chl-a (0.7–0.9 mg m^{-3}; Fig. 1h), with elevated diatoms (Fig. S4h), indicative of localized new production[44]. Cyanobacteria were observed primarily in the western basin, consistent with previous reports[45]. The 20°C isotherm was shallower than in fall (75-110 m) and deepened westward (Fig. 1e,f), closely tracking the deep chlorophyll maximum from 50 m in the east to 80 m in the west. Integrated primary productivity was different compared to fall 2019 in the east (319 ± 105 mg C m^{-2} d^{-1}), similar in the central (339 ± 90 mg C m^{-2} d^{-1}) region, and substantially lower in the west (231 ± 85 mg C m^{-2} d^{-1}). Seasonal differences between fall and spring were statistically significant (*p-value<0.05)* in the eastern and western regions (Table S2).

Overall, these observations reveal strong seasonal contrasts in nutrient supply and productivity in the EA, driven by wind-forced nitracline shoaling, EUC depth variations, and turbulent mixing[31].

Particle size distribution and carbon export dynamics

Observations from the UVP5, which imaged particles between 0.102 mm and 16.4 mm in Equivalent Spherical Diameter[46], revealed that during both cruises, particle abundances were highest at the surface and decreased with depth (Fig. 2). Small particles (MiP, 0.1-0.5 mm) were mostly found in the upper 1000 m (Fig. S5a,b), while large particles (MaP, 0.5-16 mm) were carried deeper, reaching the seafloor. Carbon export events were identified from flux anomalies (Methods) and linked to three dominant processes (Fig. 2g,h, S6): 1) seasonal upwelling, 2) TIWs, and 3) horizontal advection of particles from the continental margin via the NBC retroflection and the EUC. An enhanced particulate matter signal below 1500 m in the western EA might result from resuspension and lateral advection of small particles by the deep western boundary current (Fig. S7, supplementary text S7).

1. **Seasonal upwelling and TIWs modulate carbon export dynamics**

The occurrence of the three productivity events that led to chl-a accumulation during fall is consistent with the three peaks in the MaP concentration (Fig. 2c, S5c). Hovmöller diagrams (Fig. 2a,c,e,g) indicate that the first two upwelling events already started to weaken at the time of sampling, whereas the third was more recent and likely still active. Together, these events likely supplied particulate material for both particle size classes (MiP and MaP), consistent with phytoplankton as the primary source[47,48]. The fall cruise, conducted during a period of enhanced chl-a values, likely captured conditions favorable for particle production, aggregation, and subsequent export to depth. Two of the upper-ocean export events, roughly between 0–15°W and 25–30°W, extended down to the seafloor at 4000-5000 m depth. In contrast, the third productivity event, observed around 35°W, was confined to the upper 1000 m (Fig. 2c).

In contrast, during spring, a diatom-dominated bloom in the east led to only weak export of POC between 0–10°W (Fig. 2b,d,f,h, S4). Although diatoms efficiently form aggregates[49], satellite observations indicate that the bloom began only a few days before sampling, suggesting that aggregation and export processes were still developing. In the EA, aggregate formation and downward flux typically unfold over ~15-20 days[21,50].

Therefore, in the eastern transect, observed low export efficiency likely reflected either early bloom dynamics or enhanced carbon recycling by zooplankton[51,52].

In summary, upwelling-triggered blooms produce a fast-sinking flux of MaPs that reaches bathypelagic depths on timescales of weeks to months consistent with reported sinking velocities of large aggregates[53,54]. This deep-reaching particle flux is highly dynamic, featuring distinct seasonal pulses, episodic deposition events, and marked interannual variability[21,55]. MaP, with relatively high estimated sinking velocities, have a focused export route with minimal lateral dispersion[16,56,57], while MiPs show more variable export patterns.

2. The horizontal advection of slowly sinking particles from the continental margin via the NBC retroflection and the EUC

Anomalously high MiP concentrations were detected during spring in the western EA (Fig. 3b), where integrated productivity measurements indicate comparatively lower biological activity during this season (suppl. Table.2, Fig. S3). This particle-rich layer extended from the shallow EUC core to 150 m and was associated with pronounced downward export to deeper layers, despite the absence of detectable surface blooms or upwelling-driven nitrate supply[31]. During the observation period, the EUC core lay above the nitracline and transported nitrate-poor water eastward, excluding particle formation and export from local surface production[31]. A distinct subsurface MiP maximum was observed between 15°W and 40°W (Fig. 3d), centered at around 60 m depth within the EUC core (velocities > 0.96 m s^{-1}). The westernmost strong increase in MiP abundance at 40°W directly coincides with the location where the EUC turns in at the equator from the Northwest (Fig. 3d). We hypothesize that the MiP enrichment arises from horizontal advection of small, slowly sinking or suspended particles within the EUC, originating from source regions within the supply waters of the EUC at the continental margin.

Circulation pathways and particle sources supplying the EUC

To assess this hypothesis, we analyzed currents within the EUC density range ($24.8 < \sigma_\theta < 25.3$ kg.m^{-3}; Schott et al.[58]) using GLORYS reanalysis data and compared them with MiP distributions from Atlantic cruises (2019–2023; Fig. 4). Fall conditions are represented by 2019 (Sep-Oct) GLORYS data, coinciding with two research cruises conducted during boreal fall (Table 1), while spring (Apr-May) is reflected by a broader multi-year average (2021–2023) aligned with four boreal spring cruises (Table 1), coinciding with the availability of shipboard particle size data.

In fall (Fig. 5a), the NBC follows the Brazilian coast from 5°S, passes the Amazon shelf, and reaches 8°N, where part of the flow retroflects southeastward[59] (Fig. 4a). This retroflection becomes pronounced when the NBC is unstable, diverting flow southeastward rather than continuing northwestward[60]. It acts as a primary source of water masses, channeling thermocline/central water masses from subtropical subduction regions of the South Atlantic toward the eastern basin[59]. At 5°N, this southeastward flow bifurcates: a stronger branch feeds the North Equatorial Counter Current (NECC), while the other weaker branch veers toward the equator near 40°W, consistent with Argo float observations[60]. During boreal fall, limited MiP near the equator may also reflect supply from westward currents north and south of the EUC. Integrated MiP abundance within this water mass remained relatively low and constant during fall but increased between 4°N and 6°N at 35°W, within the NECC (Fig. S8). This pattern likely reflects enhanced northwestward and subsequent southeastward transport of particles associated with the intensified NBC retroflection, promoting further offshore and southwestward export of particles beyond the sampling region north of 5°N[61–64].

In spring (Fig. 5b), the NBC also flows northward along the northeastern coast of Brazil. The southward migration of the Intertropical Convergence Zone (ITCZ) weakens trade winds and surface divergence[25,65]. As a consequence, the NBC retroflection weakens[66], and is directed toward ~2.5°N before the water mass is injected into the EUC near 40°W (Fig. 5b). This retroflection into the EUC, which during this period is at its seasonally shallowest position, is only dominant from winter to spring[58,67].

During both fall and spring, as the NBC passes close to the continental shelf, it interacts with resuspended particles from the seabed: strong mean and tidal currents in this shallow region maintain suspended material within the frictional bottom boundary layer, preventing sediment burial and enhancing resuspension[68,69]. This promotes entrainment of suspended material into the NBC and the EUC [70–74] with particles following the NBC pathway toward ~8°N in fall and ~2.5°N in spring before injection into different eastward flows.

Backward particle-trajectory simulations using GLORYS velocity fields reveal a rapid connection between the NBC and the EUC in spring, with NBC-mediated entrainment of shelf particles into the EUC (Fig. S9). In fall, transport times exceed 40 days, implying that many sinking particles would not remain suspended long enough to reach the EUC. Assuming sinking speeds of 10–20 m d^{-1} [53,54]and EUC velocities (~1 m s^{-1}), and aggregate lifetimes of only a few weeks[75,76], efficient transfer into the EUC is therefore unlikely in fall. In spring, the short NBC-EUC connection time allows particles to be entrained into the EUC at shallow depths (50–200 m) before sinking or degradation.

The presence of the coastal holoplanktonic species *Belzebub faxoni* in spring, together with the backward-tracking analysis, supports a shelf origin of particles in the EUC (Fig. S9) at this time. *B. faxoni* is generally associated with eutrophic, low-salinity coastal waters[77] and the Amazon River plume. Although offshore occurrences have been reported[62,78], de Santana et al.[63] providing high-resolution taxonomic identification across all larval stages confirmed that its distribution remains primarily related to coastal/plume-influenced waters. The presence of adult *B. faxoni* in our dataset near the equator at 38°W, far from the continental margin, therefore indicates advective transport of coastal material into the EUC.

In summary, we suggest that cross-shelf exchanges driven by the NBC retroflection transport particulate matter to the western tropical Atlantic in both seasons but with a strong equatorial impact during spring (Fig. S11). This lateral supply enhances MiP concentrations within and below the EUC at the equator between 40°W and 15°W during spring.

Relative importance of POC supply mechanisms

To put the obtained values into context, we examined POC sources in the upper layer of the EA between 35°W and 15°W, a longitudinal range defined here for the box-based budget analysis (Fig. S10). These sources include carbon fixation through primary production and lateral advection of organic matter from the EUC at 35°W. POC losses from this layer are represented by lateral advection at 15°W and downward export of particulate carbon (Fig S9).

We estimated POC flux for different particle size classes: MaP (>0.5 mm), MiP (0.102–0.5 mm), and small extrapolated MiP (0.0508–0.102 mm), following Baudena et al.[79]. The small particle extrapolation was carried out as a sensitivity test rather than to produce definitive flux values. To validate the extrapolation, UVP-based POC flux estimates were compared with 234Th-based fluxes for particles >51 µm during spring (Fig. S12). Regional mean fluxes from extended size spectra were closely aligned (35.9 mg C m^{-2} d^{-1} from UVP vs 31.6 mg C m^{-2} d^{-1} from 234Th). The comparison was made at the regional scale due to fundamental differences in how the two approaches characterize particle flux. The 234Th method provides an integrated measure of particle flux over time (24 days, Anand et al.[80]), while the UVP captures vertically resolved episodic or localized snapshots of particle size distribution and abundance[81], that 234Th may underestimate [82].

POC fixation in the defined box during spring (153 ± 45 ktC day^{-1}) was slightly lower than in fall (179± 55 ktC day^{-1}), yet the vertical export flux was two times higher in spring when using the extrapolated budget, compared with 1.6 times higher for the standard budget (Fig. S10). Lateral POC input during spring at 35°W was 11.5 ktC day^{-1}, equivalent to 42.2 kt CO_2 or the emission of 12 average-sized coal-fired power plants (Wu et al.[83], 3.6 kt CO_2 day^{-1} for China). This shows that lateral export fluxes, often overlooked in the oligotrophic EA, can reach magnitudes comparable to major anthropogenic sources, emphasizing their importance for regional carbon transport and the global carbon cycle. During spring, MiP accounted for ~94% of total POC flux in the upper 200 m, with 70% of this from extrapolated small particles (Fig. 5).

Conclusion

In this study, we propose that particle export in the EA is shaped not only by seasonally driven vertical processes such as upwelling, mixing and TIW activity but also by a lateral subsurface transport of small particles during boreal spring. Observations from two equatorial trans-Atlantic cruises reveal a distinct seasonal contrast: strong upwelling and TIWs in fall promote phytoplankton production and deep export of large particles. Conversely, in spring, elevated concentrations of small particles in the central basin are exported despite low surface productivity. This decoupling of particle export from local primary production in spring suggests a dominant role of horizontal advection in maintaining particle and hence likely also carbon supply to the deep-sea during nutrient-limited periods. This mechanism is likely also important for the bathypelagic and -benthic community along the equator, which according to our data receives food supply further to the West and during a different season than expected based on satellite data analysis alone.

Figures

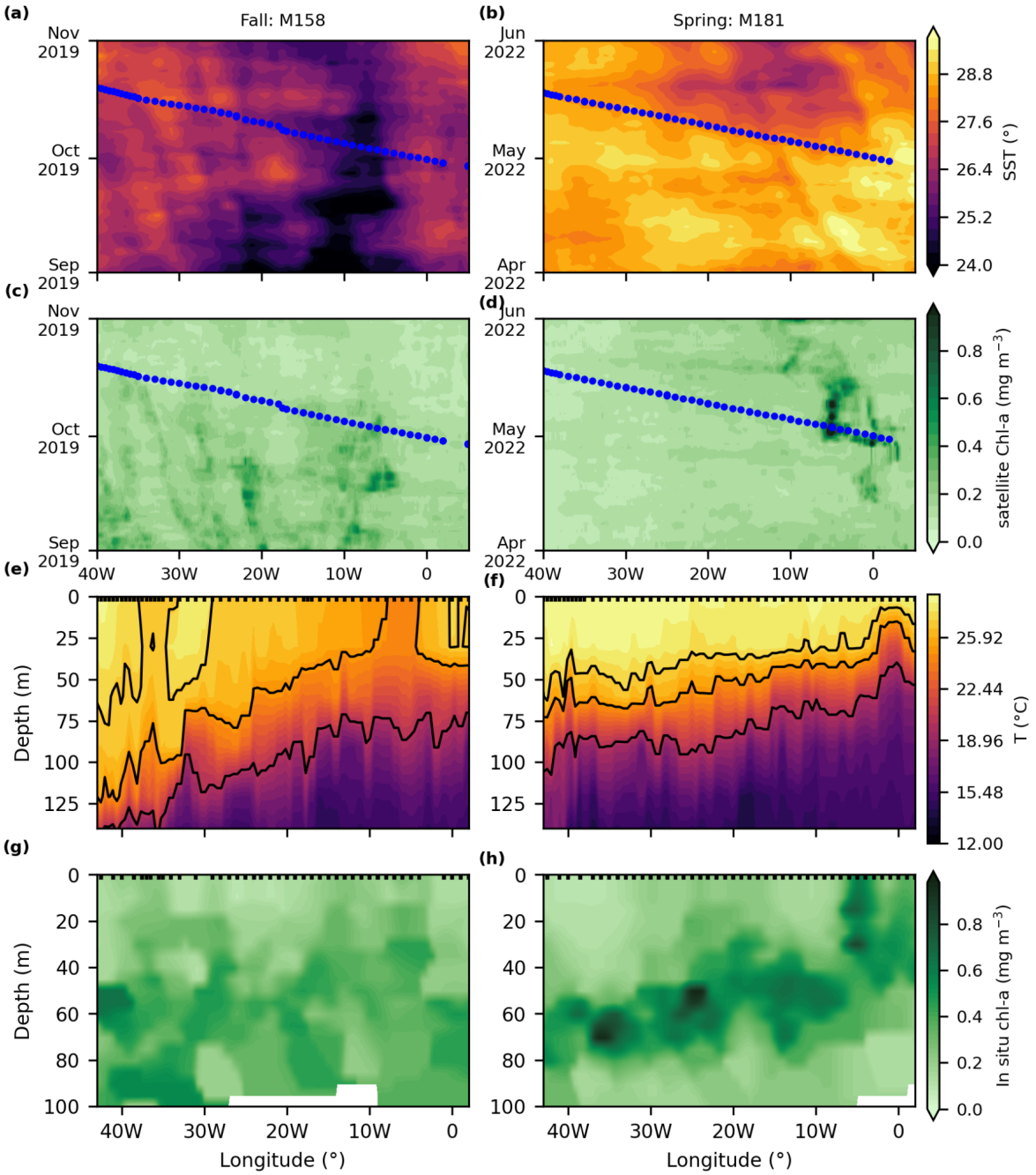


Fig. 1: Hovmöller diagrams of (a,b) satellite SST and (c,d) satellite surface chlorophyll-*a* concentration between 1°N and 1°S. (e,f) Upper-ocean temperature from the shipboard CTD sensor, and (g,h) In situ chlorophyll-*a* concentration from HPLC. The blue dotted lines represent the ship tracks of the conducted campaigns in the equatorial region. The black contour lines in (e) and (f) represent three isotherms: 27, 25, and 20 °C from the surface to the deep. Black dots in (e,f,g,h) indicate the locations of the vertical profiles sampled during the cruises.

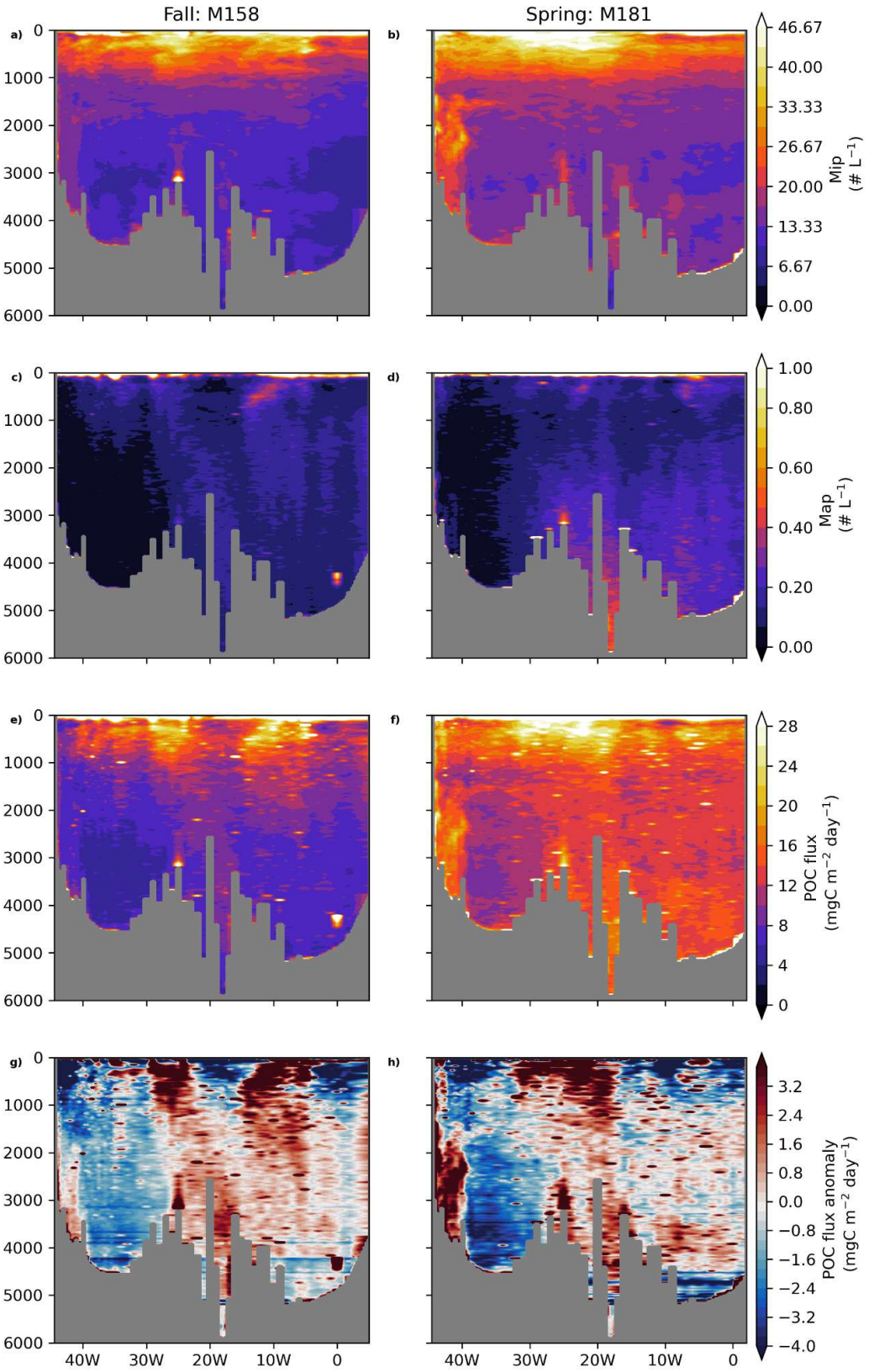


Fig. 2: Zonal distribution of particle size composition in the Equatorial Atlantic. (a,c,e,g) and (b,d,f,h) refer to the trans-Atlantic crossings in fall and spring, respectively. (a,b) Micrometric Particles (MiP) abundance (# L^{-1}), (c,d) Macroscopic Particles (MaP) abundance (# L^{-1}), (e,f) POC flux (mgC m^{-2} day^{-1}), and (g,h) POC flux anomaly during the two trans-Atlantic crossings. The x-axis limits differ between the cruises because the fall cruise started at 5°E, while the spring cruise only started at 2°E.

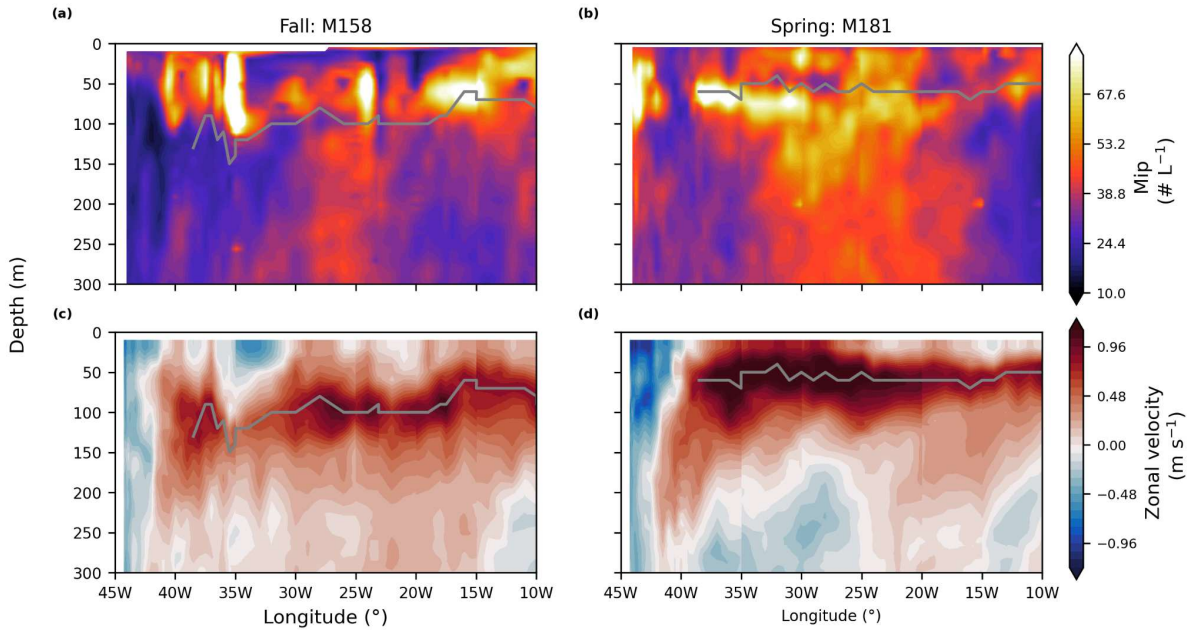


Fig. 3: Micrometric particle (MiP) abundance (# L^{-1}) and zonal (east-west) velocity ($m.s^{-1}$) in the Equatorial Atlantic. (a,c) and (b,d) refer to the trans-Atlantic crossings in fall and in spring, respectively. The grey line represents the depth of the EUC core. The longitude ranges differ from the previous panels in order to focus on the central and western Atlantic regions. Eastward/westward current velocity values are represented in red/blue.

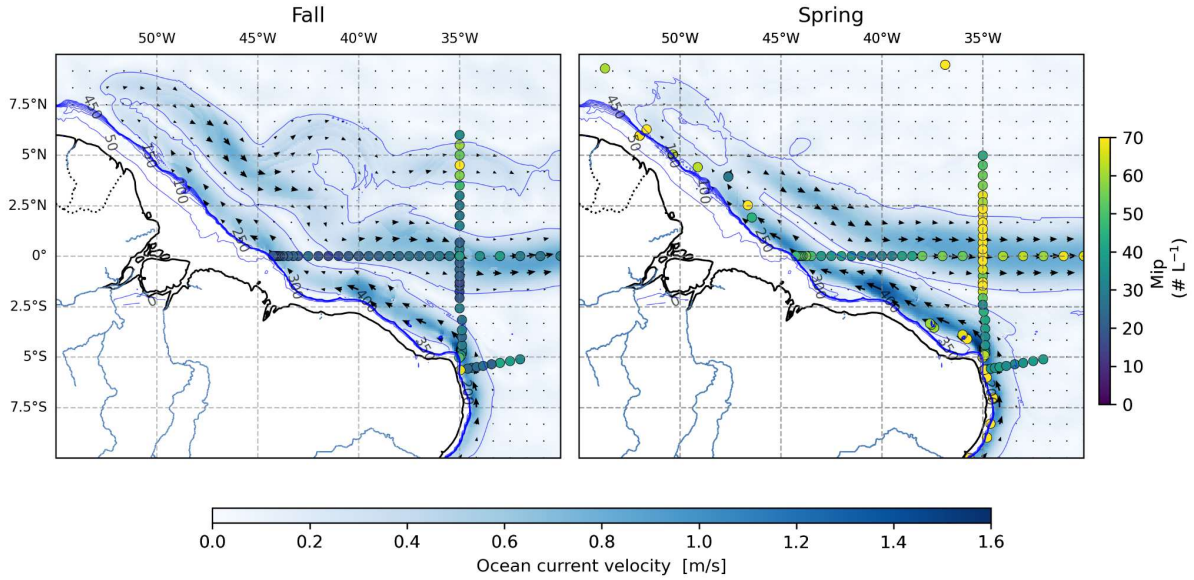


Fig. 4: Mean circulation of the Equatorial Undercurrent (EUC) during fall (September–November) 2019 and spring (April–May) averaged from 2021 to 2023, derived from model GLORYS12V1(Global Ocean Physics Reanalysis). Contour lines show an ocean current velocity between 0.15 and 0.2 m s^{-1}, while the blue lines are the ocean topography (between 0-500 m). The arrows represent the mean current velocity, with arrow length proportional to velocity magnitude. Colored dots indicate the mean abundance of micrometric particles (MiP) within the EUC for each cruise conducted in this region. The EUC is defined here by potential density layers between 24.5 and 26.3 kg m^{-3}, and MiP abundances are extracted within the same density range. The years shown in each panel are selected based on the availability of MiP observations from cruises conducted during those periods.

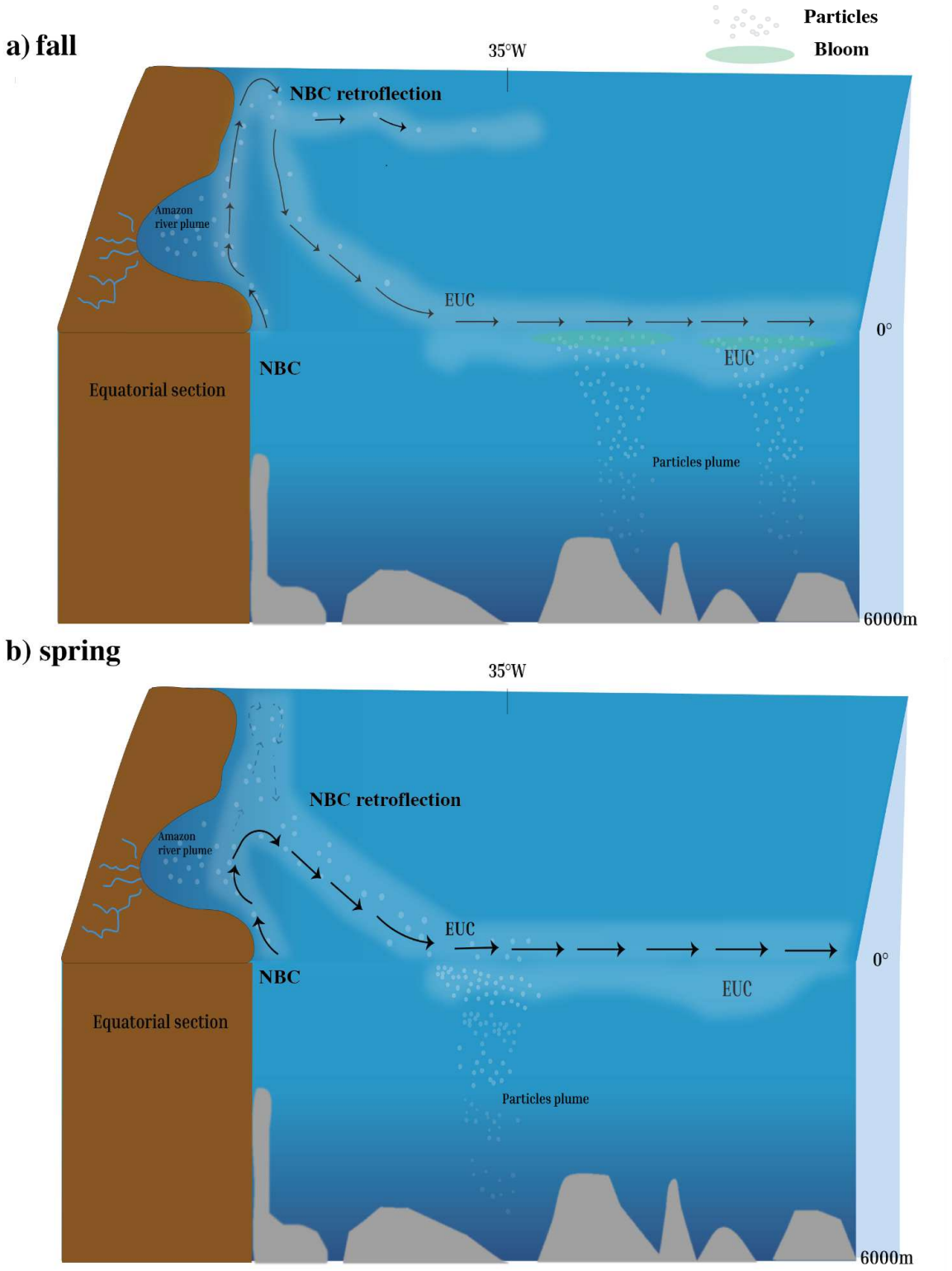


Fig. 5 Schematic of the seasonal contrast in particle transport and export in the Equatorial Atlantic. **(A)** Fall conditions. **(B)** Spring conditions. The upper panels illustrate the subsurface circulation at EUC depth of the North Brazil Current (NBC) from the western boundary to its entry into the EUC at the equatorial Atlantic, whereas the lower panel is the equatorial vertical section at 0° starting at the depth of the EUC. Shading represents the extent of the currents and arrows show their direction. white dots are particles, and green hues are phytoplankton blooms.

Material and Method

1 Satellite data

Sea Surface Temperature (SST) data were downloaded from the NOAA OI-SST data set (Huang et al[84]; https://psl.noaa.gov/data/gridded/data.noaa.oisst.v2.highres.html). The gridded data are available daily from 1981 to the present at a horizontal resolution of 0.25°. Chlorophyll-*a* (chl-a) concentrations were obtained from the Global Ocean Color product (OCEANCOLOUR_GLO_BGC_L4_MY_009_104, https://doi.org/10.48670/moi-00281) produced by ACRI-ST. The temporal resolution for both products is one day, with a spatial resolution of 4 km.

2 Model reanalysis

The water velocity, seawater salinity, and potential temperature were extracted from GLORYS12V1 (Global Ocean Physics Reanalysis), distributed by the Copernicus Marine Service (product ID: GLOBAL_MULTIYEAR_PHY_001_030). This product has a 1/12° horizontal resolution and 50 depth levels. It covers the altimetry period from 1993 onward. The model component used is the NEMO OGCM in the ORCA025 configuration forced at the surface by ECMWF ERA-Interim reanalysis. We used the datasets from cmems_mod_glo_phy_my_0.083deg_P1M-m and cmems_mod_glo_phy_myint_0.083deg_P1M-m, which contain the monthly mean fields of the 3D potential temperature, salinity, and currents information from top to bottom. Assimilated observations are in situ temperature and salinity profiles, satellite SST, and along-track sea-level anomalies obtained from satellite altimetry. More information about data assimilation can be found at https://doi.org/10.48670/moi-00021.

3 Equatorial cruise data

In this study, we use data collected during two cruises measuring along the equatorial Atlantic from east to west. These measurements were carried out as part of R/V Meteor cruise M158 (https://doi.pangaea.de/10.1594/PANGAEA.952354) from September 29 to October 22, 2019 (boreal fall season), and as part of R/V Meteor cruise M181 (https://doi.pangaea.de/10.1594/PANGAEA.952520) from April 30 to May 20, 2022 (boreal spring season). To better understand sinking organic particles, Underwater Vision Profilers (UVP5)[85] were mounted on the shipboard CTD frames to acquire particle data and images during descent. This tool sizes and counts marine particles[46] from 0.102 mm to 16.4 mm in Equivalent Spherical Diameter. The UVP provided the number of particles per liter for depth bins of 2.5 m along the water column. Particles were divided into two categories based on their size: small particles (Micrometric particles, MiP) for particles between 0.1-0.5 mm, and big particles (Macroscopic particles, MaP) between 0.5-16 mm. Carbon flux for a given size class was estimated assuming the empirical relationship between particle size and sinking speed of Kriest (2002, Ref. 9 in their Table 2), which synthesizes observations across a range of natural and experimental particle aggregates. This relationship, which has been adopted in previous studies using UVP5 observations (e.g., Kiko et al.[16]) best reproduced profiles of marine snow and particulate aggregates at the same time. A ship acoustic doppler current profiler (ADCP) measured upper ocean velocity along the ship track. During M158, velocities along the equator were measured by a 75-kHz Teledyne RDI Ocean Surveyor ADCP providing velocity distributions in the upper 650 m depth. During M181, velocities were measured by a 75-kHz Teledyne RDI Longranger ADCP providing velocity distribution in the upper 250 m depth. Both instruments provided velocities with a vertical resolution of 8 m with the shallowest measurement in 17 m depth. More information can be found in the method section of Brandt et al.[31]. Additionally, temperature and salinity measurements were collected with a Seabird CTD. The location of the profiles can be seen in Fig. S1. The chlorophyll a in vivo fluorescence profiles were obtained using a fluoremeter mounted on the CTD rosette. During cruise M181, the sensor malfunctioned and fluorescence data were therefore unavailable. Samples of HPLC pigments determinations were acquired at discrete depths and analyzed. The concentration of total chlorophyll a as determined by HPLC actually refers to the concentration of the total chlorophyll a. This measurement is an estimate of the total phytoplankton biomass. Primary production integrated from the surface to the deep chlorophyll maximum (DCM) at all stations sampled during the M158 (fall 2019) and M181 (spring

2022) cruises were also calculated. The calculation was done using trapezoidal integration of in situ primary production profiles from surface to the deep chlorophyll maximum (30-110 m depending on the region).

4 Particle abundance and flux anomalies

To identify export events, we examined anomalies of carbon flux and particle abundance. For each sampling period, we first averaged all particle-abundance profiles and all carbon-flux profiles over the entire water column to obtain a mean vertical profile for that period. Then, for every individual profile, we subtracted this mean profile from it. The result is an anomaly profile that shows how much each profile deviates from the typical vertical structure during that period.

5 Data collected from other cruises

In addition to the two trans-Atlantic equatorial cruises, we analyzed UVP5 data from other research cruises (1 cruise in boreal fall, 3 cruises in boreal spring) conducted in the Atlantic Ocean between 10°S and 10°N. For these cruises, we extracted MiP abundances within the EUC density range ($24.8 < \sigma_\theta < 25.3$; Schott et al., 2004) for the spring and fall seasons. A full list of cruises, including dates and longitudinal coverage, is provided in Supplementary Table 1.

6 Backtracking

Virtual particles were initially distributed uniformly across the equatorial Undercurrent core into the Atlantic Ocean at 35°W (same longitude and date as one of the campaign stations) for fall 2019 and spring 2022. Particles were initialised in a circular buffer of 0.1° radius around the release location.This choice was done to smooth potential errors in the velocity field, consistently with previous studies[79,87,88]. These were advected using a Runge-Kutta scheme of order 4-5 for 45 days backward in time. The velocity field used for the advection is the Copernicus product GLORYS12V1 at 78m depth. This product has a 1/12° horizontal resolution and 50 depth levels and has a daily temporal resolution.

7 Estimating POC supply between 15-35°W

We defined a study region from 15–35°W to assess the POC supply entering and leaving the system. We assume that the region at 35°W, with a width of 2° in the north-south direction, serves as the productive source sustaining the increase in particle abundance. We use 200 m as the upper boundary of the twilight zone. The sources of organic carbon in this layer include carbon fixation through primary production and eastward lateral advection at 35°W, while the loss of carbon in this layer is due to the lateral advection of carbon at 15°W and the downward vertical export of particulate carbon. The vertically integrated primary production was calculated by trapezoid integration down to the DCM in all stations where at least two depths were available, and then averaged over the section. Particulate organic carbon concentration for each size class was calculated by combining particle abundance from UVP data with estimated carbon flux. Fluxes were derived using an empirical particle size–sinking speed relationship from Kriest et al.[86]. Extrapolation to particles <0.102 mm was performed using the slope of the particle size distribution when statistically significant, extending estimates down to 0.058 mm. This method was already validated by Baudena et al.[79]. POC content of particles was calculated for each of the three groups: MaP POC content (particles>0.5 mm), MiP POC content (particles between 0.102-0.5mm), and small extrapolated MiP POC content (particles between 0.0508-0.102mm). The resulting POC content was then multiplied by the monthly mean current velocity from GLORYS (0.5 m s^{-1} for M181, at 35°W), which constituted the lateral flux input at 35°W. The average ocean current velocity of the area was estimated from the GLORYS velocity field. We also compared the model velocities with those estimated from ADCP measurements for M181 and found good agreement in current speeds. Therefore, we use the GLORYS values to represent the mean in the following. A vertical downward flux was also calculated at 200 m between 15-35°W. This analysis does not account for the lateral exit of POC along the northern and southern boundaries, downward mixing of dissolved organic carbon, or active transport by vertical migration of zooplankton, due to data limitations.

Data availability

CTD data are available on PANGEA; the DOI can be found in the supplementary material (Table 1). CTD data from cruise MSM117 are available on Zenodo and data used in this manuscript for the carbon flux and particle concentrations are available online using the following DOI: https://github.com/joellehabib/TRATLEQ12_26. Further data can be made available by the authors upon request.

Code availability

All necessary code for the data analysis and the preparation of the figures are available on Github at https://github.com/joellehabib/TRATLEQ12_26. Budget calculation scripts can be made available by J. Habib upon request.

Acknowledgements

The study was supported by EU H2020 under grant agreement 817578 TRIATLAS project and by the Deutsche Forschungsgemeinschaft through several research cruises with R/V Meteor and R/V Maria S. Merian. RK acknowledges support via a Make Our Planet Great Again grant from the French National Research Agency (ANR) within the Programme d'Investissements d'Avenir #ANR-19-MPGA-0012 and funding from the Heisenberg Programme of the German Science Foundation #KI 1387/5-1. AFC was supported by Xunta de Galicia Postdoctoral Fellowship ED481D 2017/0061, and Beatriz Galindo fellowship BG22-00067. We thank the captains, crews, scientists, and technicians involved in several research cruises in the tropical Atlantic that contributed to collecting data used in this study.

References

1. Kulk, G. *et al.* Primary Production, an Index of Climate Change in the Ocean: Satellite-Based Estimates over Two Decades. *Remote Sens.* **12**, 826 (2020).

2. Henson, S. A. *et al.* A reduced estimate of the strength of the ocean's biological carbon pump: BIOLOGICAL CARBON PUMP STRENGTH. *Geophys. Res. Lett.* **38**, n/a-n/a (2011).

3. Ocean Carbon Pumps: Analysis of Relative Strengths and Efficiencies in Ocean-Driven Atmospheric CO_2 Changes. *Geophys. Monogr. Ser.* 99–110 (1985) doi:10.1029/gm032p0099.

4. Passow, U. & Carlson, C. The biological pump in a high CO<sub>2 world. *Mar. Ecol. Prog. Ser.* **470**, 249–271 (2012).

5. Alldredge, A. L. & Silver, M. W. Characteristics, dynamics and significance of marine snow. *Prog. Oceanogr.* **20**, 41–82 (1988).

6. Guidi, L. *et al.* Effects of phytoplankton community on production, size, and export of large aggregates: A world‐ocean analysis. *Limnol. Oceanogr.* **54**, 1951–1963 (2009).

7. Jackson, R. B. *et al.* Trading Water for Carbon with Biological Carbon Sequestration. *Science* **310**, 1944–1947 (2005).

8. Riley, J. S. *et al.* The relative contribution of fast and slow sinking particles to ocean carbon export. *Glob. Biogeochem. Cycles* **26**, (2012).

9. Buesseler, K. O. & Boyd, P. W. Shedding light on processes that control particle export and flux attenuation in the twilight zone of the open ocean. *Limnol. Oceanogr.* **54**, 1210–1232 (2009).

10. Giering, S. L. C. *et al.* Reconciliation of the carbon budget in the ocean's twilight zone. *Nature* **507**, 480–483 (2014).

11. Siegel, D. A. *et al.* Global assessment of ocean carbon export by combining satellite observations and food‐web models. *Glob. Biogeochem. Cycles* **28**, 181–196 (2014).

12. Stemmann, L., Jackson, G. A. & Gorsky, G. A vertical model of particle size distributions and fluxes in the midwater column that includes biological and physical processes—Part II: application to a three year survey in the NW Mediterranean Sea. *Deep Sea Res. Part Oceanogr. Res. Pap.* **51**, 885–908 (2004).

13. Baudena, A. *et al.* A Lagrangian perspective reveals the carbon and oxygen budget of an oceanic eddy. *Commun. Earth Environ.* **6**, (2025).

14. Dall'Olmo, G. & Mork, K. A. Carbon export by small particles in the Norwegian Sea. *Geophys. Res. Lett.* **41**, 2921–2927 (2014).

15. Durkin, C. A., Estapa, M. L. & Buesseler, K. O. Observations of carbon export by small sinking particles in the upper mesopelagic. *Mar. Chem.* **175**, 72–81 (2015).

16. Kiko, R. *et al.* Biological and physical influences on marine snowfall at the equator. *Nat. Geosci.* **10**, 852–858 (2017).

17. Clements, D. J. *et al.* Constraining the Particle Size Distribution of Large Marine Particles in the Global Ocean With In Situ Optical Observations and Supervised Learning. *Glob. Biogeochem. Cycles* **36**, e2021GB007276 (2022).

18. Trull, T. W. *et al.* In situ measurement of mesopelagic particle sinking rates and the control of carbon transfer to the ocean interior during the Vertical Flux in the Global Ocean (VERTIGO) voyages in the North Pacific. (2008).

19. Wang, X., Murtugudde, R., Hackert, E. & Marañón, E. Phytoplankton carbon and chlorophyll distributions in the equatorial Pacific and Atlantic: A basin-scale comparative study. *J. Mar. Syst.* **109–110**, 138–148 (2013).

20. Grodsky, S. A., Carton, J. A. & McClain, C. R. Variability of upwelling and chlorophyll in the equatorial Atlantic. *Geophys. Res. Lett.* **35**, (2008).

21. Habib, J. *et al.* Marine snow surface production and bathypelagic export at the Equatorial Atlantic from an imaging float. *Biogeosciences* **22**, 7985–8003 (2025).

22. Longhurst, A. Seasonal cooling and blooming in tropical oceans. *Deep Sea Res. Part Oceanogr. Res. Pap.* **40**, 2145–2165 (1993).

23. Westberry, T. K., Silsbe, G. M. & Behrenfeld, M. J. Gross and net primary production in the global ocean: An ocean color remote sensing perspective. *Earth-Sci. Rev.* **237**, 104322 (2023).

24. Radenac, M.-H. *et al.* Physical drivers of the nitrate seasonal variability in the Atlantic cold tongue. *Biogeosciences* **17**, 529–545 (2020).

25. Brandt, P. *et al.* Physical processes and biological productivity in the upwelling regions of the tropical Atlantic. *Ocean Sci.* **19**, 581–601 (2023).

26. Perez, V., Fernández, E., Marañón, E., Serret, P. & Garcia-Soto, C. Seasonal and interannual variability of chlorophyll a and primary production in the Equatorial Atlantic: in situ and remote sensing observations. *J. Plankton Res.* **27**, 189–197 (2005).

27. Tuchen, F. P. *et al.* Modulation of Equatorial Currents and Tropical Instability Waves During the 2021 Atlantic Niño. *J. Geophys. Res. Oceans* **129**, e2023JC020431 (2024).

28. Brandt, P., Funk, A., Tantet, A., Johns, W. E. & Fischer, J. The Equatorial Undercurrent in the central Atlantic and its relation to tropical Atlantic variability. *Clim. Dyn.* **43**, 2985–2997 (2014).

29. Giarolla, E., Nobre, P., Malagutti, M. & Pezzi, L. P. The Atlantic Equatorial Undercurrent: PIRATA observations and simulations with GFDL Modular Ocean Model at CPTEC. *Geophys. Res. Lett.* **32**, (2005).

30. Hormann, V. & Brandt, P. Atlantic Equatorial Undercurrent and associated cold tongue variability. *J. Geophys. Res.* **112**, C06017 (2007).

31. Brandt, P. *et al.* Seasonal productivity of the equatorial Atlantic shaped by distinct wind-driven processes. *Nat. Geosci.* **18**, 84–90 (2025).

32. Signorini, S. R. *et al.* Biological and physical signatures in the tropical and subtropical Atlantic. *J. Geophys. Res. Oceans* **104**, 18367–18382 (1999).

33. Brandt, P. *et al. Trans-Atlantic Equatorial Cruise I, Cruise No. M158, September 19 - October 26, 2019, Walvis Bay (Namibia) - Recife (Brazil)*. *METEOR-Berichte* vol. M158 1–48 https://www.tib.eu/suchen/id/awi:a382cf8b90dfdbc17fc5e26ba2fa05c781631250 (2019).

34. Brandt, P. *et al. Trans-Atlantic Equatorial Cruise II, Cruise No. M181, April 17 - May 28, 2022, Cape Town (South Africa) - Mindelo (Cape Verde)*. *METEOR-Berichte* vol. M181 1–52 https://www.tib.eu/suchen/id/awi:2f0131752665dabe0fa3b369b5de972e1ae06550 (2022).

35. Richter, I., Tokinaga, H. & Okumura, Y. M. The Extraordinary Equatorial Atlantic Warming in Late 2019. *Geophys. Res. Lett.* **49**, (2022).

36. Lee, S. *et al.* On the Genesis of the 2021 Atlantic Niño. *Geophys. Res. Lett.* **50**, e2023GL104452 (2023).

37. Fischer, G., Ratmeyer, V. & Wefer, G. Organic carbon fluxes in the Atlantic and the Southern Ocean: relationship to primary production compiled from satellite radiometer data. (2000).

38. Wefer, G. & Fischer, G. Seasonal patterns of vertical particle flux in equatorial and coastal upwelling areas of the eastern Atlantic. *Deep Sea Res. Part Oceanogr. Res. Pap.* **40**, 1613–1645 (1993).

39. Brandt, P. *et al.* Equatorial upper‐ocean dynamics and their interaction with the West African monsoon. *Atmospheric Sci. Lett.* **12**, 24–30 (2011).

40. Sherman, J. *et al.* The Photophysiological Response of Nitrogen-Limited Phytoplankton to Episodic Nitrogen Supply Associated With Tropical Instability Waves in the Equatorial Atlantic. *Front. Mar. Sci.* **8**, 814663 (2022).

41. Foltz, G. R., Hummels, R., Dengler, M., Perez, R. C. & Araujo, M. Vertical Turbulent Cooling of the Mixed Layer in the Atlantic ITCZ and Trade Wind Regions. *J. Geophys. Res. Oceans* **125**, e2019JC015529 (2020).

42. Heukamp, F. O. *et al.* Tropical Instability Waves and Wind‐Forced Cross‐Equatorial Flow in the Central Atlantic Ocean. *Geophys. Res. Lett.* **49**, e2022GL099325 (2022).

43. Moum, J. N. *et al.* Deep Cycle Turbulence in Atlantic and Pacific Cold Tongues. *Geophys. Res. Lett.* **49**, e2021GL097345 (2022).

44. Sarthou, G., Timmermans, K. R., Blain, S. & Tréguer, P. Growth physiology and fate of diatoms in the ocean: a review. *J. Sea Res.* **53**, 25–42 (2005).

45. Fernández, A., Mouriño-Carballido, B., Bode, A., Varela, M. & Marañón, E. Latitudinal distribution of *Trichodesmium* spp. and N_2 fixation in the Atlantic Ocean. *Biogeosciences* **7**, 3167–3176 (2010).

46. Kiko, R. *et al.* A global marine particle size distribution dataset obtained with the Underwater Vision Profiler 5. *Earth Syst. Sci. Data* **14**, 4315–4337 (2022).

47. Alldredge, A. PARTICLE AGGREGATION DYNAMICS. (2001).

48. Alldredge, A. L., Granata, T. C., Gotschalk, C. C. & Dickey, T. D. The physical strength of marine snow and its implications for particle disaggregation in the ocean. *Limnol. Oceanogr.* **35**, 1415–1428 (1990).

49. Kiørboe, T., Lundsgaard, C., Olesen, M. & Hansen, J. L. S. Aggregation and sedimentation processes during a spring phytoplankton bloom: A field experiment to test coagulation theory. *J. Mar. Res.* **52**, 297–323 (1994).

50. Henson, S. A., Yool, A. & Sanders, R. Variability in efficiency of particulate organic carbon export: A model study. *Glob. Biogeochem. Cycles* **29**, 33–45 (2015).

51. Henson, S., Le Moigne, F. & Giering, S. Drivers of Carbon Export Efficiency in the Global Ocean. *Glob. Biogeochem. Cycles* **33**, 891–903 (2019).

52. Ward, B. A., Dutkiewicz, S. & Follows, M. J. Modelling spatial and temporal patterns in size-structured marine plankton communities: top–down and bottom–up controls. *J. Plankton Res.* **36**, 31–47 (2014).

53. Soviadan, Y. D. *et al.* Marine snow morphology drives sinking and attenuation in the ocean interior. *Biogeosciences* **22**, 3485–3501 (2025).

54. Stemmann, L., Gorsky, G., Marty, J.-C., Picheral, M. & Miquel, J.-C. Four-year study of large-particle vertical distribution (0–1000m) in the NW Mediterranean in relation to hydrology, phytoplankton, and vertical flux. *Deep Sea Res. Part II Top. Stud. Oceanogr.* **49**, 2143–2162 (2002).

55. Beaulieu, S. E. Accumulation and fate of phytodetritus on the sea floor. (2002).

56. Bach, L. T. *et al.* The Influence of Plankton Community Structure on Sinking Velocity and Remineralization Rate of Marine Aggregates. *Glob. Biogeochem. Cycles* **33**, 971–994 (2019).

57. Turner, J. T. Zooplankton fecal pellets, marine snow, phytodetritus and the ocean's biological pump. *Prog. Oceanogr.* **130**, 205–248 (2015).

58. Schott, F. A., Mccreary, J. P. & Johnson, G. C. Shallow Overturning Circulations of the Tropical-Subtropical Oceans. in *Geophysical Monograph Series* 261–304 (American Geophysical Union, Washington, D. C., 2004). doi:10.1029/147GM15.

59. Hazeleger, W., De Vries, P. & Friocourt, Y. Sources of the Equatorial Undercurrent in the Atlantic in a High-Resolution Ocean Model. *J. Phys. Oceanogr.* **33**, 677–693 (2003).

60. Tuchen, F. P., Brandt, P., Lübbecke, J. F. & Hummels, R. Transports and Pathways of the Tropical AMOC Return Flow From Argo Data and Shipboard Velocity Measurements. *J. Geophys. Res. Oceans* **127**, e2021JC018115 (2022).

61. Araujo, M. *et al.* A Synoptic Assessment of the Amazon River-Ocean Continuum during Boreal Autumn: From Physics to Plankton Communities and Carbon Flux. *Front. Microbiol.* **8**, 1358 (2017).

62. De Santana, C. S. *et al.* Amazon river plume influence on planktonic decapods in the tropical Atlantic. *J. Mar. Syst.* **212**, 103428 (2020).

63. De Santana, C. S., Hauss, H., Schwamborn, R. & Kiko, R. Horizontal distribution of mesozooplankton biomass and size spectra along the Amazon River plume continuum during the mesoscale North Brazil current retroflection. *J. Plankton Res.* **47**, fbaf048 (2025).

64. Varona, H. L., Veleda, D., Silva, M., Cintra, M. & Araujo, M. Amazon River plume influence on Western Tropical Atlantic dynamic variability. *Dyn. Atmospheres Oceans* **85**, 1–15 (2019).

65. Xie, S.-P. & Carton, J. A. Tropical Atlantic Variability: Patterns, Mechanisms, and Impacts. in *Geophysical Monograph Series* (eds Wang, C., Xie, S. P. & Carton, J. A.) 121–142 (American Geophysical Union, Washington, D. C., 2013). doi:10.1029/147GM07.

66. Dimoune, D. M., Birol, F., Hernandez, F., Léger, F. & Araujo, M. Revisiting the tropical Atlantic western boundary circulation from a 25-year time series of satellite altimetry data. *Ocean Sci.* **19**, 251–268 (2023).

67. Didden, N. & Schott, F. Eddies in the North Brazil Current retroflection region observed by Geosat altimetry. *J. Geophys. Res. Oceans* **98**, 20121–20131 (1993).

68. Kuehl, S. A., Nittrouer, C. A. & DeMaster, D. J. Modern sediment accumulation and strata formation on the Amazon continental shelf. *Mar. Geol.* **49**, 279–300 (1982).

69. Tchilibou, M. *et al.* Internal tides off the Amazon shelf during two contrasted seasons: interactions with background circulation and SSH imprints. *Ocean Sci.* **18**, 1591–1618 (2022).

70. Bao, R. *et al.* Organic Carbon Aging During Across‐Shelf Transport. *Geophys. Res. Lett.* **45**, 8425–8434 (2018).

71. Hollister, C. D. & Nowell, A. R. M. Prologue: Abyssal storms as a global geologic process. *Mar. Geol.* **99**, 275–280 (1991).

72. Hwang, J., Druffel, E. R. M. & Eglinton, T. I. Widespread influence of resuspended sediments on oceanic particulate organic carbon: Insights from radiocarbon and aluminum contents in sinking particles. *Glob. Biogeochem. Cycles* **24**, (2010).

73. Hwang, J. *et al.* Biological and physical controls on the flux and characteristics of sinking particles on the Northwest Atlantic margin. *J. Geophys. Res. Oceans* **122**, 4539–4553 (2017).

74. Karakaş, G. *et al.* High‐resolution modeling of sediment erosion and particle transport across the northwest African shelf. *J. Geophys. Res. Oceans* **111**, (2006).

75. Iversen, M. H. & Ploug, H. Ballast minerals and the sinking carbon flux in the ocean: carbon-specific respiration rates and sinking velocity of marine snow aggregates. *Biogeosciences* **7**, 2613–2624 (2010).

76. Ploug, H. Small‐scale oxygen fluxes and remineralization in sinking aggregates. *Limnol. Oceanogr.* **46**, 1624–1631 (2001).

77. Longhurst, A. R. & Pauly, D. *Ecology of Tropical Oceans*. (Academic Press, San Diego, 1987).

78. Fugimura, M. M. S., Oshiro, L. M. Y. & Silva, R. DISTRIBUIÇÃO E ABUNDÂNCIA DAS FAMÍLIAS LUCIFERIDAE E SERGESTIDAE (CRUSTACEA, DECAPODA, NATANTIA) NA BAÍA DE SEPETIBA, RIO DE JANEIRO, BRASIL. . *p.* **25**,.

79. Baudena, A. *et al.* A Lagrangian perspective reveals the carbon and oxygen budget of an oceanic eddy. *Commun. Earth Environ.* **6**, 318 (2025).

80. Anand, S., Rengarajan, R. & Sarma, V. V. S. S. ^{234}Th‐Based Carbon Export Flux Along the Indian GEOTRACES GI02 Section in the Arabian Sea and the Indian Ocean. *Glob. Biogeochem. Cycles* **32**, 417–436 (2018).

81. Buesseler, K. O., Boyd, P. W., Black, E. E. & Siegel, D. A. Metrics that matter for assessing the ocean biological carbon pump. *Proc. Natl. Acad. Sci.* **117**, 9679–9687 (2020).

82. Arellano, A. R. *et al.* Mechanisms of Organic Matter Export in Estuaries with Contrasting Carbon Sources. *J. Geophys. Res. Biogeosciences* **124**, 3168–3188 (2019).

83. Wu, N. *et al.* Daily Emission Patterns of Coal-Fired Power Plants in China Based on Multisource Data Fusion. *ACS Environ. Au* **2**, 363–372 (2022).

84. Huang, B. *et al.* Improvements of the Daily Optimum Interpolation Sea Surface Temperature (DOISST) Version 2.1. *J. Clim.* **34**, 2923–2939 (2021).

85. Picheral, M. *et al.* The Underwater Vision Profiler 5: An advanced instrument for high spatial resolution studies of particle size spectra and zooplankton. *Limnol. Oceanogr. Methods* **8**, 462–473 (2010).

86. Kriest, I. Different parameterizations of marine snow in a 1D-model and their influence on representation of marine snow, nitrogen budget and sedimentation. *Deep Sea Res. Part Oceanogr. Res. Pap.* **49**, 2133–2162 (2002).

87. Ser-Giacomi, E. *et al.* Lagrangian betweenness as a measure of bottlenecks in dynamical systems with oceanographic examples. *Nat. Commun.* **12**, 4935 (2021).

88. Baudena, A. *et al.* Fine-scale structures as spots of increased fish concentration in the open ocean. *Sci. Rep.* **11**, 15805 (2021).

Supplementary Files

This is a list of supplementary files associated with this preprint. Click to download.

- Supplementaryinformation2026.pdf